1

Use of Oxide Ligands in Designing Catalytic Active Sites

*Edward L. Lee** and Israel E. Wachs*

1.1
Introduction

Oxides of the group 5–7 metals (V, Nb, Ta, Cr, Mo, W, and Re) supported on a high surface area oxide material (SiO_2, Al_2O_3, TiO_2, ZrO_2, etc.) are recognized as industrially important catalysts for numerous chemical reactions [1–11]. For example, these catalysts are utilized for *o*-xylene oxidation to phthalic anhydride [12, 13], methane/methanol oxidation to formaldehyde [14], and selective catalytic reduction (SCR) of NO with ammonia to N_2 over supported vanadia catalysts [15–19]; SCR of NO with ammonia and selective oxidation of methane over supported molybdena catalysts [20–22]; olefin metathesis and hydrocarbon isomerization reactions over tungsta catalysts; and metathesis of olefins and alkanes over supported rhenia catalysts [23–25]. These supported metal oxide catalysts consist of highly dispersed surface metal oxide species – the catalytic active sites – anchored to the underlying oxide support. Over the decades, there have been many successful methods of controlling and anchoring the molecularly dispersed metal oxide phase by chemical vapor deposition (CVD) [26–28], incipient wetness impregnation [29–34], and precipitation [35–37]. The surface coverage of the metal oxide overlayer can vary from below to above monolayer coverage or the maximum dispersion limit, that is, maximum metal oxide dispersion before formation of crystalline metal oxide nanoparticles (NPs). Below monolayer surface coverage, only surface isolated (or monomeric) and surface polymeric metal oxide species are present on the support. At low surface coverage, only isolated surface metal oxide species are generally present [38]. Above monolayer coverage or maximum dispersion limit, crystalline metal oxide NPs are also present and reside on top of the molecularly dispersed surface metal oxide monolayer. Therefore, monolayer coverage or maximum dispersion limit is a critical parameter that allows distinguishing between two-dimensional molecularly dispersed surface metal oxide species and the three-dimensional NPs

*Present Work Address: The Dow Chemical
Company Core Research and Development
1776 Building, Midland, MI 48674, USA

present in supported metal oxide materials. For the purposes of simplifying and focusing the discussion, only SiO_2-supported metal oxide catalysts at submonolayer coverages will be discussed in this chapter since the catalysis literature has demonstrated that only isolated surface metal oxide species are present at low coverage for supported MO_x/SiO_2 catalysts [14, 38–56].

The surface metal oxide species of supported metal oxide catalysts control the overall catalytic performance such as activity and selectivity. Thus, understanding the interactions of the surface metal oxide catalytic active sites with their environment (e.g., the underlying oxide support material and reactive environments) provides the ability to control and design these catalytic active sites. By spreading the catalytic active oxide layer over the underlying oxide support layers, the interfacial interaction of these "monolayer" catalysts results in different structures and catalytic properties than their bulk metal oxide counterparts [57, 58]. Therefore, recent studies have focused on characterizing the bridging M−O−support bond for the design and control of the catalytic performance. The focus of this chapter will be to systematically surface modify the SiO_2 support with surface AlO_x, TiO_x, and ZrO_x species (the oxide ligands). The group 5–7 transition metal oxides (V_2O_5, MoO_3, and Re_2O_7) will then be anchored onto the surface-modified SiO_2 support by means of incipient wetness impregnation of soluble precursors and calcination. The V_2O_5, MoO_3, and Re_2O_7 catalytic active sites were chosen because of their dominant redox characteristics that will allow comparison of their reactivity properties. These "multilayered" supported $M_1O_x/M_2O_x/SiO_2$ catalysts will then be characterized and examined for their surface chemistry against the model supported MO_x/SiO_2 systems to understand the influence of the oxide ligands on the molecular/electronic structures and catalytic performance of the surface metal oxide species.

In keeping with the theme of the book for new approaches to synthesis and characterization of heterogeneous catalysts, this chapter will focus on the oxide ligand of the "multilayered" supported $M_1O_x/M_2O_x/SiO_2$ catalysts by characterizing the surface M_1O_x molecular and electronic structures and investigating the catalytic reactivity for oxidative dehydrogenation of methanol to formaldehyde. The molecular and electronic structures of the supported $M_1O_x/M_2O_x/SiO_2$ catalysts will be determined with *in situ* Raman and UV–Vis diffuse reflectance spectroscopy (DRS) spectroscopy, respectively, under various environments (e.g., dehydrated, oxidative, reductive, and isotopic exchange) to investigate the fundamental interactions between the surface metal oxide overlayer (M_1O_x) and the surface oxide modifiers (M_2O_x) on the silica support. Time-resolved Raman spectra for reductive and isotopic oxygen exchange studies will provide additional insights into the dynamic nature of these catalytic active sites. The catalytic surface reactivity will be chemically probed via CH_3OH temperature-programmed surface reaction (CH_3OH-TPSR) spectroscopy that will provide the surface kinetics and nature of the catalytic active sites (redox, acidic, or basic). Theoretical modeling results via computational density functional theory (DFT) from the literature will be referenced where appropriate. This systematic approach to supported metal oxide catalysts will assist in the establishment of molecular structure–reactivity relationship for designing and controlling surface metal oxide catalytic active sites.

1.2
Molecular Structural Determination of Supported Metal Oxide Catalysts with *In Situ* Raman Spectroscopy

Raman spectroscopic studies in the late 1970s first reported the detection of surface metal oxide species for supported MoO$_3$ [59–61], WO$_3$ [62], V$_2$O$_5$ [63, 64], and Re$_2$O$_7$ [65] catalysts. These studies were followed by *in situ* Raman measurements in the early 1980s, where the gas phase environment and temperature of the catalyst could be controlled [66–70]. Detection of the reversible surface structures when exposed to hydrated and dehydrated conditions was demonstrated during this period [66]. These earlier experimental breakthroughs and with further advances in Raman technology allowed for the characterization of the surface structures of mixed metal oxide catalysts [58]. New approaches for *in situ* Raman spectroscopic measurements of catalytic surfaces are now undertaken via measurements under reductive, isotopic D$_2$O$-$H$_2$O and ^{16}O$-^{18}$O exchange environments coupled with time-resolved spectroscopy. These approaches provide new fundamental insights that enable the molecular structural determination of the catalytic active surface metal oxide sites present in supported metal oxide catalysts.

It is important to recall that isotopic ^{16}O$-^{18}$O exchange results in band splitting. Based on vibrational theory, monoxo species are expected to exhibit two Raman vibrations (M$=^{16}$O and M$=^{18}$O); dioxo species are projected to give rise to three Raman vibrations (^{16}O$=$M$=^{16}$O, ^{18}O$=$M$=^{16}$O, and ^{18}O$=$M$=^{18}$O); and trioxo species are expected to exhibit four Raman vibrations (M$(=^{16}$O$)_3$, ^{18}O$=$M$(=^{16}$O$)_2$, $(^{18}$O$=)_2$M$=^{16}$O, and M$(=^{18}$O$)_3$) [71–75]. The position of the vibrational shifts can be estimated using a simple M$-$O diatomic oscillator model for the isotopic ratio:

$$
\begin{bmatrix} \nu_{O-M}^{16} \\ \nu_{O-M}^{18} \end{bmatrix} = \frac{\frac{1}{2\pi c}\sqrt{\left(k\left(\frac{1}{m_M}+\frac{1}{m_{16}}\right)\right)}}{\frac{1}{2\pi c}\sqrt{\left(k\left(\frac{1}{m_M}+\frac{1}{m_{18}}\right)\right)}} = \frac{\sqrt{\left(\frac{1}{m_M}+\frac{1}{m_{16}}\right)}}{\sqrt{\left(\frac{1}{m_M}+\frac{1}{m_{18}}\right)}} \tag{1.1}
$$

where ν is the frequency of the M$-$O bond (cm^{-1}), k is the force constant, and m is the mass of the transition metal ion or oxygen [71, 73].

1.3
Characterization of AlO$_x$, TiO$_x$, and ZrO$_x$ Surface-Modified SiO$_2$

The surface of SiO$_2$ was modified by the deposition on the surface of M$_2$O$_x$ (AlO$_x$, TiO$_x$, or ZrO$_x$) species. For each supported M$_2$O$_x$/SiO$_2$ system, the surface-modified SiO$_2$ support consists of 5% M$_2$O$_x$/SiO$_2$, which is below the maximum dispersion limit for these oxides on SiO$_2$. The *in situ* Raman spectra of the dehydrated supported M$_2$O$_x$/SiO$_2$ samples are presented in Figure 1.1 (left) and do not exhibit any new significant spectral features as compared to the original SiO$_2$ support, with the exception of TiO$_x$/SiO$_2$, which will be discussed below. The deposition of alumina, titania, and zirconia on the silica support causes a decrease in the intensity of the band
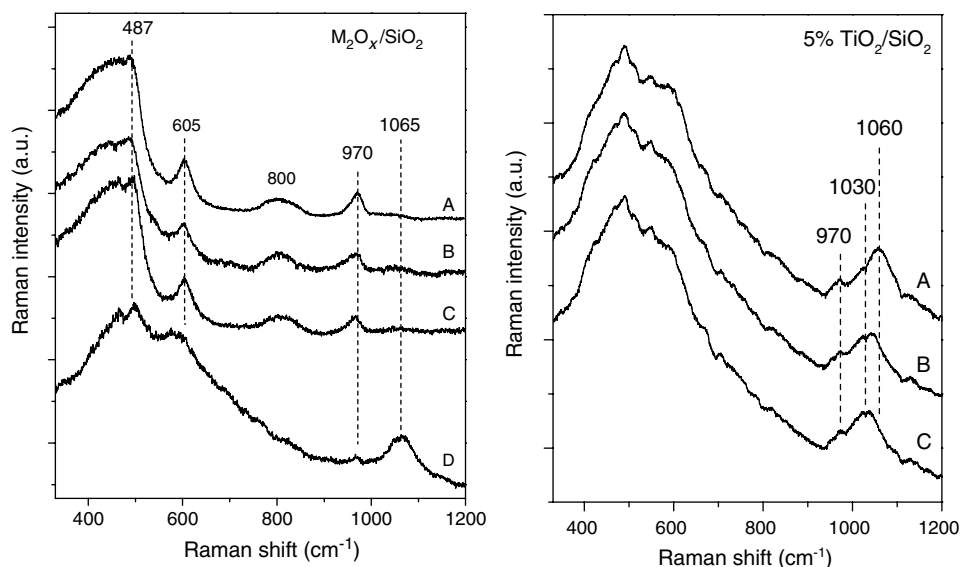
Figure 1.1 (Left) *In situ* Raman spectra of (A) pure and unmodified
SiO$_2$ and surface-modified SiO$_2$ with (B) 5% ZrO$_x$, (C) 5% AlO$_x$, and
(D) 5% TiO$_x$ oxide ligands using 325 nm excitation energy at 500 °C.
(Right) Time-resolved *in situ* Raman spectra of 5% TiO$_x$/SiO$_2$
during H$_2$^{18}O exposure after (A) 0 min, (B) 30 min, and (C) 80 min.

at 970 cm^{-1} of the Si−OH vibration and indicates consumption of the Si−OH surface
hydroxyls. This decrease is further confirmed by *in situ* near-IR DRS at 7315 cm^{-1} (2ν).
The surface modification of the SiO$_2$ surface by the deposited oxides leads to direct
interactions with the silica surface hydroxyl groups, resulting in the broadening of the
970 cm^{-1} band, and in the ZrO$_2$/SiO$_2$ spectrum, its shift toward lower wavenumbers
(∼940 cm^{-1}), which is suggestive of bridging Zr−O−Si linkages. Therefore, the AlO$_x$,
ZrO$_x$, and TiO$_x$ surface modifiers anchor to the silica at the Si−OH site to create a
surface metal oxide layer with residual exposed Si−OH species also present.

Additional Raman features are present, however, for the supported TiO$_x$/SiO$_2$
sample in Figure 1.1 (left). The transverse-optical (TO) mode of the silica network at
1065 cm^{-1}, assigned to perturbed Si(−O$^-$)$_2$ and Si−O$^-$ silica vibrations from the
formation of Ti−O−Si bridging bond, appears to be resonance Raman enhanced
with the 325 nm excitation, and the broad band at 550–600 cm^{-1} is suggestive of a
small amount of polymeric Ti−O−Ti species. The supported TiO$_x$/SiO$_2$ sample was
exposed to isotopic ^{18}O$_2$ and monitored with time-resolved *in situ* Raman, see
Figure 1.1 (right), to determine if the ∼1065 cm^{-1} band is related to the TO mode
of the silica network or possibly the Ti=O bond. The isotopic oxygen exchange
resulted in the band shift from ∼1060 to ∼1030 cm^{-1}, which exactly corresponds to
that of the TO vibration [76] since Ti=^{18}O should shift to 1015 cm^{-1} for a simple
Ti−O diatomic oscillator (see Equation 1.1).

Extensive characterization experiments under dehydrated conditions have also
been conducted by means of *in situ* IR, UV–Vis DRS, XPS, XANES, and ^{27}Al NMR,

which provide additional molecular information about the supported MO_x phases on SiO_2 [77–80]. The supported 5% TiO_2/SiO_2 and 5% ZrO_2/SiO_2 samples consist of 100% dispersed surface TiO_x and ZrO_x species on the SiO_2 support. The surface TiO_x species are present as TiO_4 and TiO_5 coordinated species and the former dominates at the lower TiO_x content (such as 5% TiO_2/SiO_2). The coordination environments of the dehydrated surface ZrO_x species have yet to be determined. The supported 5% Al_2O_3/SiO_2 sample primarily contains surface AlO_4 coordination with a minor amount of surface AlO_5 species [77]. In summary, supported 5% TiO_2/SiO_2 sample consists of $(OH)-Ti-(O-Si)_3$, and the 5% Al_2O_3/SiO_2 consists of $(O^-)-Al-(O-Si)_3$ where the extra proton (Bronsted acid site) is on the bridging oxygen in the $Al-O-Si$ bond.

1.4
Anchoring Site of Surface M₁Oₓ Species on Supported M₂Oₓ/SiO₂

The supported M_1O_x phases are all found to be present as two-dimensional surface metal oxide species on the M_2O_x/SiO_2 supports, as will be shown below with Raman spectroscopy. The anchoring site of the surface M_1O_x species takes place on exposed surface $-OH$ sites and is related to the acidic/basic nature of the surface $-OH$ groups. It is well established that anchoring of acidic surface M_1O_x initially occurs at the most basic surface $-OH$ groups, followed by the neutral surface $-OH$ groups, and finally, the most acidic surface $-OH$ groups [81]. The acidity of the surface $-OH$ groups is related to the electronegativity of the oxide support cation and increases with the support cation electronegativity ($Zr \sim Ti < Al < Si$) [82]. Consequently, the acidic surface M_1O_x species preferentially anchor to the more basic surface $Zr-OH$, $Ti-OH$, and $Al-OH$ sites over the more acidic surface $Si-OH$ sites. This preferential anchoring is best demonstrated by the Raman spectra of the supported WO_x/SiO_2 and $WO_x/AlO_x/SiO_2$ catalytic systems, as shown in Figure 1.2. The supported WO_3/SiO_2 gives rise to a dominant Raman band at 982 cm^{-1} (dioxo $v_s(W(=O)_2)$) and a minor Raman band at 1014 cm^{-1} (monoxo $v_s(W=O)$) that transform to monoxo $v_s(W=O)$ species with a Raman band at 1020 cm^{-1} for the supported $WO_3/Al_2O_3/SiO_2$ catalyst system. Furthermore, the monoxo $v_s(W=O)$ Raman band position at 1020 cm^{-1} matches that for monoxo $v_s(W=O)$ species present in the supported WO_3/Al_2O_3 catalysts [83]. These Raman spectral changes clearly reflect the preferential anchoring of the surface WO_x species at the surface AlO_x sites over exposed SiO_2 sites on the surface-modified SiO_2 support. The preferential anchoring of the surface M_1O_x species at the surface M_2O_x species over the exposed SiO_2 support sites is a general phenomenon for anchoring of group 5–7 transition metal oxides on the surface-modified SiO_2 support.

1.5
Molecular Structure of Dehydrated Supported V₂O₅/SiO₂ and V₂O₅/M₂Oₓ/SiO₂ Catalyst Systems

The surface vanadium oxide species in the dehydrated V_2O_5/SiO_2 catalyst exhibit a sharp and intense Raman vibration at 1038 cm^{-1}, as shown in Figure 1.3 (left), curve
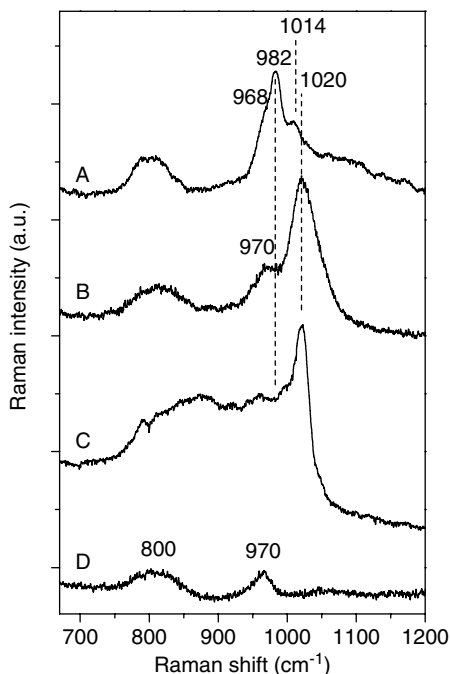
Figure 1.2 *In situ* Raman spectra under oxidizing conditions using 532 nm excitation energy of (A) 6% WO_3/SiO_2, (B) 3% $WO_3/5\%$ Al_2O_3/SiO_2, (C) 20% WO_3/Al_2O_3, and (D) pure SiO_2 for reference.

labeled A, and has been assigned to the terminal $\nu_s(V{=}O)$ stretch of isolated surface VO_4 species [39–45]. This Raman band position is also independent of exposure to D_2O at elevated temperatures indicating that there are no V−OH functionalities (not shown for brevity). The position of the terminal V=O vibration at $1038\,\mathrm{cm}^{-1}$ is consistent with the monoxo V=O structure present in $H_3SiMo_{11}VO_{40}$ Keggin structure ($1034\,\mathrm{cm}^{-1}$) and $(Ph_3SiO)_3V{=}O$ ($1022\,\mathrm{cm}^{-1}$), as well as with DFT calculations (1038–$1047\,\mathrm{cm}^{-1}$) for the simple gas phase monomer structure, $O{=}V(OCH_3)_3$ and monomeric polyhedral oligomeric silsesquioxanes [84–86]. Furthermore, dioxo $O{=}V{=}O$ structures vibrate at a wavenumber $\sim$970 (ν_s)/960 (ν_{as}) cm^{-1} [73]. The terminal $\nu_s(V{=}O)$ vibration is accompanied by weaker bands at 340 and $905\,\mathrm{cm}^{-1}$, assigned to the bending (δ) V−O and stretching V−O−Si modes, respectively. The weak shoulder band at $1070\,\mathrm{cm}^{-1}$ is characteristic of the silica network TO mode and has been assigned to perturbed $Si(-O^-)_2$ and $Si{-}O^-$ silica vibrations that are also indicative of the formation of bridging V−O−Si bonds [40]. The partial reduction of the 1038, 905, and $340\,\mathrm{cm}^{-1}$ Raman bands at 600 °C under the reducing H_2 environment, shown in curve B of Figure 1.3 (left), confirms the assigned V=O, V−O−Si and bending V−O vibrations to surface V−O vibrations [43]. Comparison of the Raman spectra for the reduced supported V_2O_5/SiO_2 catalyst sample with that of the SiO_2 support (see curve C of Figure 1.3 (left)) reveals the decrease of the silica 970 and $605\,\mathrm{cm}^{-1}$ bands relative to the silica $800\,\mathrm{cm}^{-1}$ band upon deposition of
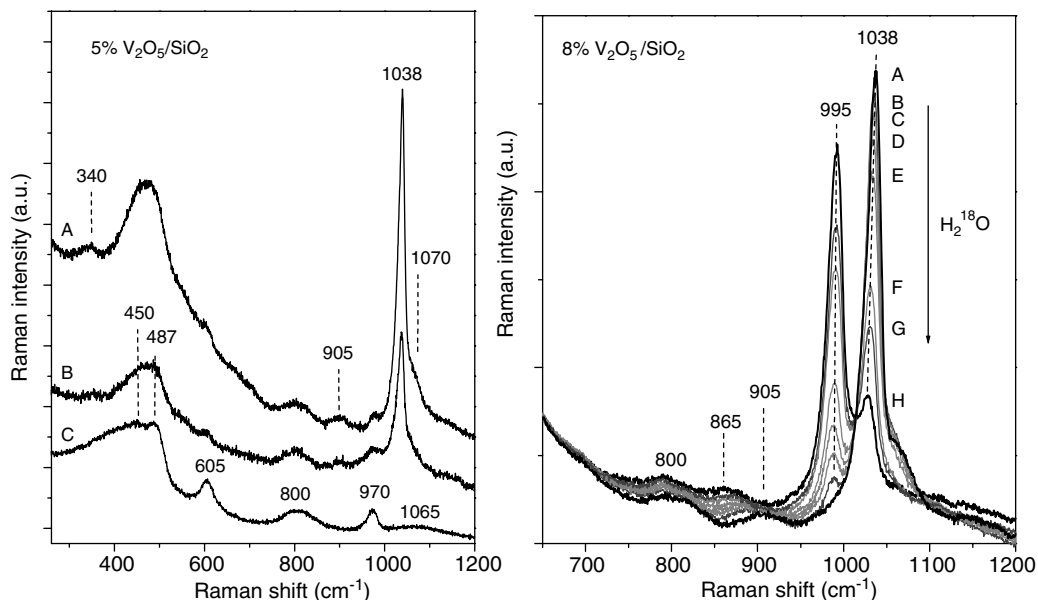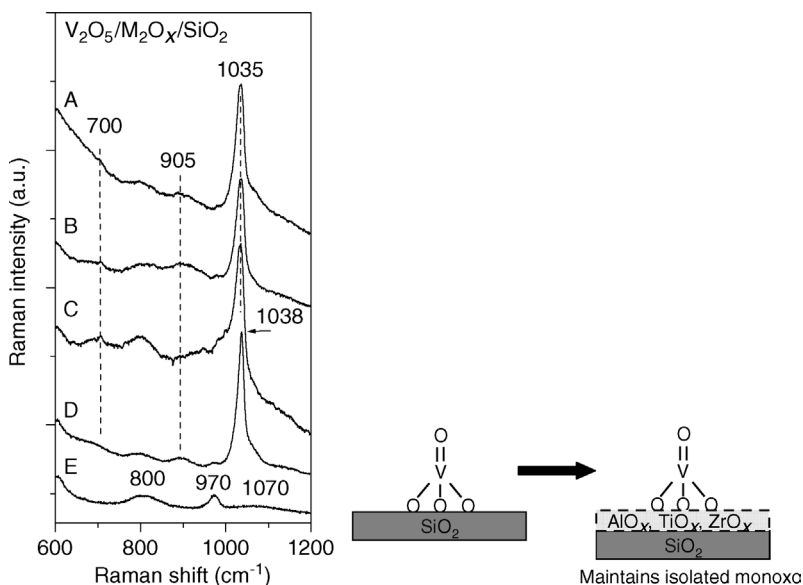
Figure 1.3 (Left) *In situ* Raman spectra of supported 5% V_2O_5/SiO_2 using 532 nm excitation energy under (A) oxidizing conditions at 450 °C and (B) hydrogen reducing conditions (5% H_2/Ar at 600 °C). The dehydrated SiO_2 support is shown for reference in (C). Reproduced from Ref. [55]. (Right) Time-resolved *in situ* Raman spectra of supported 8% V_2O_5/SiO_2 during $H_2{}^{18}O$ exposure after (A) 0 min, (B) 10 min, (C) 20 min, (D) 30 min, (E) 40 min, (F) 70 min, (G) 90 min, and (H) 130 min. Reproduced from Ref. [56].

surface vanadia species, indicating the preferential anchoring of the surface vanadia species at the isolated SiO_2 support surface hydroxyls and the three-membered siloxane rings, respectively. Deuterated water experiments result in a shift of the $970 \, cm^{-1}$ band to $\sim 955 \, cm^{-1}$ due to the exchange of Si−(OH) to Si−(OD) as seen with the pure silica [55]. Additional insight is provided by time-resolved isotopic oxygen exchange of the dehydrated supported V_2O_5/SiO_2 catalyst, shown in Figure 1.3 (right), and results in splitting of the surface V=O band to 1038 and $995 \, cm^{-1}$ (assigned to $v_s(V={}^{16}O)$ and $v_s(V={}^{18}O)$, respectively) and shifting of the V−O−Si vibration from 905 to $865 \, cm^{-1}$ [56, 72]. The time-resolved Raman spectra reveal that the two symmetric V=O bands remain at the same wavenumber during the exchange process. The shift from 1038 to $995 \, cm^{-1}$ closely matches the theoretical $V={}^{18}O$ vibration at $993 \, cm^{-1}$ of a simple diatomic oscillator model [56].

The Raman spectra of the dehydrated supported $V_2O_5/TiO_2/SiO_2$, $V_2O_5/ZrO_2/SiO_2$, and $V_2O_5/Al_2O_3/SiO_2$ catalysts are presented in Figure 1.4 (left) and give rise to a single sharp band at $\sim 1035 \, cm^{-1}$ from the $v_s(V=O)$ stretching mode of the dehydrated surface VO_x species. The similarity of the terminal $v_s(V=O)$ vibrations for the supported $VO_x/M_2O_x/SiO_2$ catalysts to that of the model supported VO_x/SiO_2 catalyst indicates that all these catalysts contain the same monoxo V=O species. The constancy of the V=O vibration indicates that the surface structure stays monoxo even with the addition of the surface modifiers, as depicted in Figure 1.4 (right).

Figure 1.4 (Left) *In situ* Raman spectra (532 nm) of dehydrated supported (A) 5% $V_2O_5/TiO_x/SiO_2$, (B) 5% $V_2O_5/ZrO_x/SiO_2$, (C) 5% $V_2O_5/AlO_x/SiO_2$, and (D) 5% V_2O_5/SiO_2 catalysts under oxidizing conditions at 600 °C. Pure dehydrated SiO_2 spectrum (E) is provided for reference. Reproduced in part from refs. [44, 77, 87–90]. (Right) Schematic of dehydrated supported VO_x species on SiO_2 and surface-modified silica.

Furthermore, there is no apparent ligand effect of the surface modifiers on the molecular structure of the surface VO_x species. A new weak Raman band at $\sim$700 cm^{-1} is also present for the supported $VO_x/M_2O_x/SiO_2$ catalysts, which becomes more intense with increasing vanadia and additive concentrations and is tentatively assigned to the stretching mode of the corresponding V−O−Al/V−O−Zr/V−O−Ti bridging bonds.

1.6
Molecular Structure of Dehydrated Supported MoO₃/SiO₂ and MoO₃/M₂Oₓ/SiO₂ Catalyst Systems

The *in situ* Raman spectrum of dehydrated supported MoO_3/SiO_2 is presented in curve A of Figure 1.5 (left). The dehydrated surface molybdenum oxide species possess dioxo $(O=)_2Mo(-O-Si)_2$ and monoxo $O=Mo(-O-Si)_4$ structures that give rise to Raman bands for $\nu_s(Mo(=O)_2)$ at $\sim$976–988 cm^{-1} and $\nu_s(Mo=O)$ at 1020 cm^{-1}, respectively [91–97]. The corresponding dioxo $\nu_{as}(Mo(=O)_2)$ stretch appears as a shoulder at 965–975 cm^{-1} and the weak vibration at 364 cm^{-1} is attributed to the bending $\delta(O-Mo-O)$ mode [20, 75, 94–97]. The surface MoO_x vibration at 1020 cm^{-1} is consistent with that of the monoxo $H_3SiMo_{12}O_{40}$ Keggin structure (1006 cm^{-1}) and DFT calculations predicting monoxo $(Si-O)_4Mo=O$ vibrations at 1014–1017 cm^{-1}.
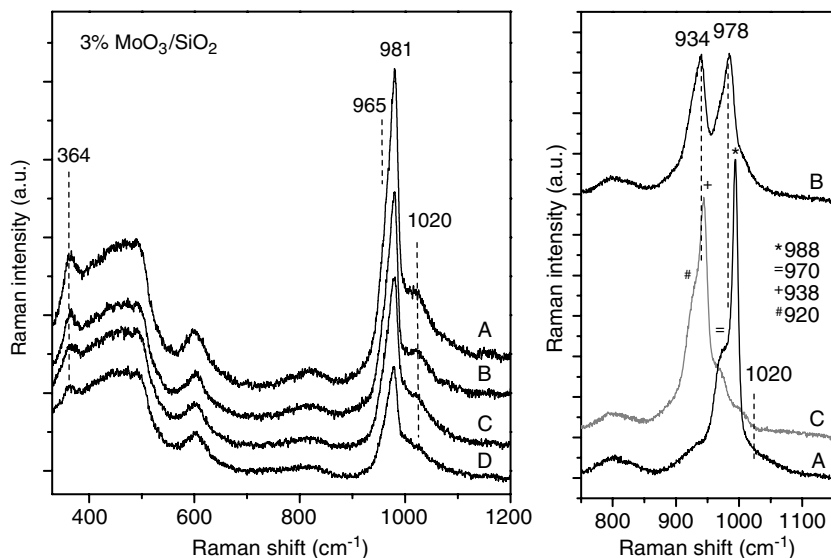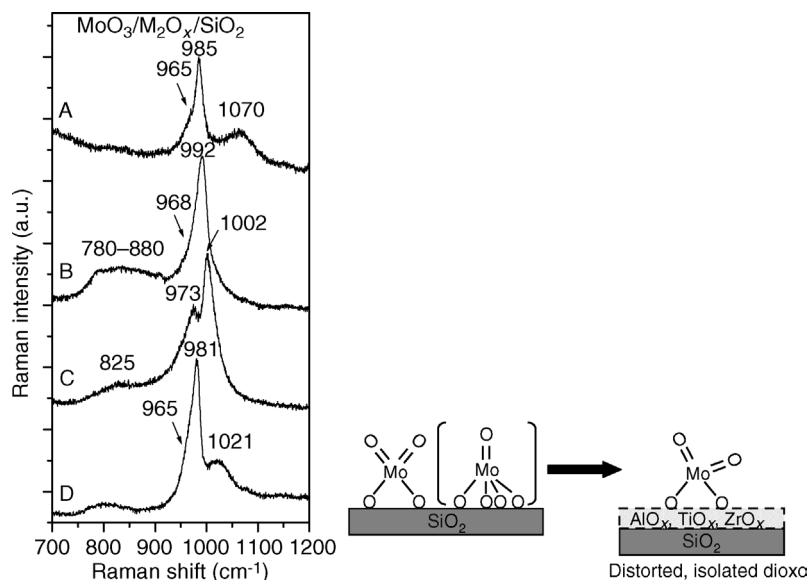
Figure 1.5 (Left) *In situ* Raman spectra (325 nm) of supported 3% MoO$_3$/SiO$_2$ under (A) oxidizing, dehydrated conditions at 500 °C, (B) reoxidation after H$_2$ exposure, (C) 2% H$_2$/He exposure, and (D) 5% H$_2$/He exposure. Reproduced from Ref. [55]. (Right) Time-resolved *in situ* Raman spectra (325 nm) of supported 8% MoO$_3$/SiO$_2$ during H$_2$^{18}O exposure after (A) 0 min, (B) 13 min, and (C) 100 min.

Consequently, the surface molybdena vibrations present for the dehydrated supported MoO$_3$/SiO$_2$ catalyst samples at 976–988 cm^{-1} with the shoulder band at 965–975 cm^{-1} correspond to dioxo surface O=Mo=O species, consistent with DFT calculations predicting the dioxo (Si−O)$_2$Mo(=O)$_2$ vibration located at 995 (v_s) and 977 (v_{as}), respectively. The expected weak bridging Mo−O−Si band is not readily observed in the ∼900–930 cm^{-1} region and may be overshadowed by the intense bands of the surface molybdena species. Upon exposure to reducing hydrogen environments, the surface v_s(Mo(=O)$_2$) vibration present in the *in situ* Raman spectrum of curve D of Figure 1.5 (left) reduces its intensity to about a quarter of the fully oxidized intensity, which indicates partial reduction. Additionally, the decrease in intensity of the Raman bands at 364, ∼965, and 1020 cm^{-1} during the H$_2$ reduction treatments confirms that these assignments are associated with Mo−O vibrations. Oxidation of the partially reduced supported MoO$_3$/SiO$_2$ catalysts restores all the surface MoO$_x$ vibrations as shown in curve B of Figure 1.5 (left).

The surface dioxo v_s and v_{as} (Mo(=^{16}O)$_2$) Raman bands at 988 and 970 cm^{-1} shift to 938 and 920 cm^{-1}, respectively, after almost complete isotopic oxygen exchange of the corresponding Mo(=^{18}O)$_2$ species, and are presented in Figure 1.5 (right). The shift of approximately −50 cm^{-1} is consistent with earlier IR literature observations, that the 990 cm^{-1} band shifts to 940 cm^{-1} during isotopic exchange from Mo^{16}O to Mo^{18}O species [97] and that the 970 cm^{-1} band shifts to 935 cm^{-1} for the Mo=^{16}O to Mo=^{18}O species [98], and with Raman spectra studies that the 988 cm^{-1} band shifts to 938 cm^{-1} [99]. The Raman band of the surface monoxo v_s(Mo=^{16}O) species at

$1020\,cm^{-1}$ is not readily observed in Figure 1.5 (right) because of resonance enhancement of the vibrations of the surface dioxo species and the presence of a greater concentration of surface dioxo species at higher MoO_x loading (8 wt.%). Consequently, only the isotopic shift of for surface dioxo species will be discussed. At intermediate extent of isotopic oxygen exchange, the band splitting occurs at $978\,cm^{-1}$ of the $\nu_s(Mo(=^{16}O)_2)$ vibration and at $934\,cm^{-1}$ of the $\nu_s(Mo(=^{18}O)_2)$ species. Note that the $\nu_s(Mo(=O)_2)$ vibration shifts from $988\,cm^{-1}$, when the surface MoO_4 contains $\sim$100% ^{16}O, to $978\,cm^{-1}$, when the surface MoO_4 is composed of a mixture of ^{16}O and ^{18}O. No shift of any surface species (Raman bands at $\sim$965, 976–991, and $1020\,cm^{-1}$) is observed during H_2O-D_2O exchange or during injection of pure H_2O, which is consistent with the absence of an Mo−OH functionality. Therefore, shifting of the Raman bands is indicative of intermediate $^{16}O=Mo=^{18}O$ species, as suggested by DFT calculations. The DFT calculations predict that the Mo=O component shows a shift of not more than 5–7 cm^{-1} (995 to $\sim$988 cm^{-1}) from $\nu_s(Mo(=^{16}O)_2)$ to $\nu_s(^{16}O=Mo=^{18}O)$ and one that is larger, $\sim$32 cm^{-1} ($\sim$988 to $\sim$956 cm^{-1}), from $\nu_s(^{16}O=Mo=^{18}O)$ to $\nu_s(Mo(=^{18}O)_2)$. Experimentally, the Mo=O component shows an initial shift of 5–10 cm^{-1} (981–988 to 976–978 cm^{-1}) followed by a larger one, of almost −40 cm^{-1}, to $\sim$933–938 cm^{-1}, which represents the shift from $\nu_s(Mo(=^{16}O)_2)$ to $\nu_s(^{16}O=Mo=^{18}O)$ to $\nu_s(Mo(=^{18}O)_2)$. The $\nu_{as}(Mo(=^{16}O)_2)$ shoulder vibration at $970\,cm^{-1}$ that shifts 40–50 cm^{-1} to lower wavenumbers also closely follows the DFT calculations, where it is predict that the shift of $\nu_{as}(Mo(=^{16}O)_2)$ to $\nu_{as}(Mo(=^{18}O)_2)$ is −43 cm^{-1} (977 to $\sim$934 cm^{-1}) after complete exchange. The shoulder at $\sim$920 cm^{-1} is also consistent with $\nu_{as}(Mo(=^{18}O)_2)$ and not the Si−^{18}OH vibration, which appears at $950\,cm^{-1}$ (not shown for brevity). Thus, consistent with predictions from the DFT calculations, the existence of the intermediate $^{16}O=Mo=^{18}O$ species allows for the conclusion that the dehydrated surface molybdenum oxide species exist as surface dioxo $O_2Mo(=O)_2$ species.

The dehydrated supported $MoO_3/TiO_x/SiO_2$, $MoO_3/ZrO_x/SiO_2$, and $MoO_3/AlO_x/SiO_2$ catalysts give rise to Raman bands in the 985–1002 cm^{-1} assigned to dehydrated surface dioxo $Mo(=O)_2$ species, and are presented in curves A, B, and C, respectively, of Figure 1.6 (left) [88, 100]. These Raman spectra do not exhibit the Raman band at $1020\,cm^{-1}$ of the isolated surface monoxo M=O species, suggesting that the surface modifiers affected the ratio of the two dehydrated surface MoO_x species. The slight shift from 981 to 985–1002 cm^{-1} indicates distortions of the dioxo surface $Mo(=O)_2$ species from interactions with the surface AlO_x, TiO_x, and ZrO_x additives on the surface-modified SiO_2 support, schematically depicted in Figure 1.6 (right). The somewhat higher wavenumber value of 1002 cm^{-1} for the supported $MoO_3/AlO_x/SiO_2$ system may reflect the presence of some monoxo surface MoO_5 species. The corresponding surface dioxo $\nu_{as}(Mo(=O)_2)$ band occurs as a shoulder at $\sim$965–975 cm^{-1} on the strong symmetric stretch and is most visible for the highly distorted supported $MoO_3/AlO_x/SiO_2$ catalyst at 973 cm^{-1}, however, surface hydroxyl groups and some surface dioxo species may also overlap in this region. The weak and broad bands at $\sim$825–880 cm^{-1} observed for supported $MoO_3/AlO_x/SiO_2$ and $MoO_3/ZrO_x/SiO_2$ catalysts are assigned to bridging M−O−Al and M−O−Zr bonds, respectively [95, 101, 102].
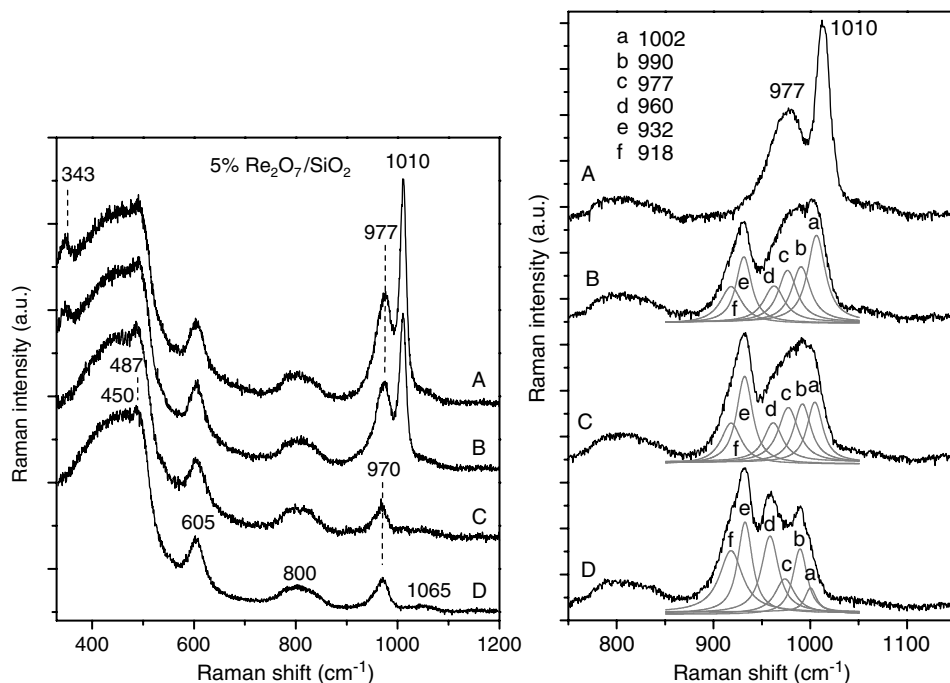
Figure 1.6 (Left) *In situ* Raman spectra (325 nm) of dehydrated supported (A) 3% $MoO_3/TiO_x/SiO_2$, (B) 3% $MoO_3/ZrO_x/SiO_2$, (C) 3% $MoO_3/AlO_x/SiO_2$, and (D) 3% MoO_3/SiO_2 under oxidizing conditions at 500 °C. (Right) Schematic of dehydrated supported MoO_x species on SiO_2 and on surface-modified silica.

1.7
Molecular Structure of Dehydrated Supported Re₂O₇/SiO₂ and Re₂O₇/M₂Oₓ/SiO₂ Catalyst Systems

The dehydrated surface rhenium oxide species on the supported Re_2O_7/SiO_2 catalyst are present as isolated trioxo surface $(O{=})_3Re{-}O{-}Si$ species, giving rise to Raman bands for $v_s(Re(=O)_3)$ at $1010 \, cm^{-1}$, $v_{as}(Re(=O)_3)$ at $977 \, cm^{-1}$, and bending $\delta(O{-}Re{-}O)$ at $343 \, cm^{-1}$. The Raman spectrum is presented in curve A of Figure 1.7 (left) [103, 104]. The $977 \, cm^{-1}$ band from the surface ReO_x species of Re_2O_7/SiO_2 overlaps with the Si$-$OH band at $970 \, cm^{-1}$, as will be further shown below. The positions of these three surface ReO_x Raman bands coincide with the $v_s(Re(=O)_3)$, $v_{as}(Re(=O)_3)$, and $\delta(O{-}Re{-}O)$ vibrations of the trioxo $Re(=O)_3$ functionality of the gas phase $(O{=})_3Re{-}O{-}Re(=O)_3$ molecule at 1009, 972, and $341 \, cm^{-1}$, respectively. However, the vibrations of the bridging Re$-$O$-$Re bond at 456 (v_s) and 185 (δ) cm^{-1} are absent, and this is consistent with the isolated nature of the surface rhenia species on the SiO_2 support. The bridging Re$-$O$-$Si band, expected to give rise to a weak band at $\sim900 \, cm^{-1}$, is not readily apparent in the vibrational spectrum. Upon exposure to reducing hydrogen environments, the dehydrated surface ReO_4 species on SiO_2 readily reduces, as shown in curve C of Figure 1.7 (left). The complete removal of the Re$-$O vibrations under reducing environments followed by complete restoration of

Figure 1.7 (Left) *In situ* Raman spectra (325 nm) of supported 5% Re_2O_7/SiO_2 under (A) oxygen environment at 450 °C, (B) reoxidation after hydrogen reduction at 2% H_2/Ar, and (C) after 40 min H_2 exposure. The SiO_2 support material is shown as reference (D). Reproduced from Ref. [55]. (Right) Time-resolved *in situ* Raman spectra of supported 5% Re_2O_7/SiO_2 under $H_2{}^{18}O$ exposure after (A) 0 min, (B) 34 min, (C) 51 min, and (D) 123 min. The Raman spectra deconvolution are shown in gray and labeled with small letters, with the lower-case letters a, b, c, d, e, and f referring to specific band positions indicated in the figure.

the Re—O vibrations under oxidizing environments (Raman bands at 1010, 977, and 343 cm^{-1}) in curve B of Figure 1.7 (left) confirms that these vibrations are associated with the surface rhenia species. Note that the Raman spectrum of the reduced supported Re_2O_7/SiO_2 catalyst looks exactly like the Raman spectrum of the dehydrated SiO_2 support and demonstrates that the SiO_2 support is not reduced by the reduction treatments. In addition, the broadening of the 977 cm^{-1} band to 968 cm^{-1} and the lack of shift of the 343 and 1010 cm^{-1} Raman bands during exposure to D_2O reflect that these vibrations are not associated with surface Re—OH species [55].

Isotopic $H_2{}^{18}O$ exchange of the dehydrated supported Re_2O_7/SiO_2 catalyst is shown in Figure 1.7 (right) and reveals the Raman band splitting of the Re(=O)$_3$ species. The initial $v_s(Re(={}^{16}O)_3)$ Raman band at 1010 cm^{-1} rapidly decreases in intensity and shifts to lower wavenumbers because of the incorporation of ^{18}O into the surface ReO_4 species and, concurrently, the $v_{as}(Re(={}^{16}O)_3)$ band at 977 cm^{-1} also shifts to lower wavenumbers. The associated bending $\delta({}^{16}O-Re-{}^{16}O)$ mode shifts from 343 to $\sim$335 cm^{-1} as a consequence of incorporation of the ^{18}O into the surface rhenia structure [56]. The time-resolved Raman spectroscopy during the isotopic oxygen

exchange allows for the resolution of the multiple band splitting of the symmetric and asymmetric vibrations, where the ν_s vibrations are deconvoluted at ~1002, 990, and ~960 cm^{-1} and the ν_{as} vibrations are deconvoluted at 932 cm^{-1}, with a small shoulder at ~918 cm^{-1}. The Raman bands at ~1002 and 990 cm^{-1} are tentatively assigned to a single substituted-^{18}O species, ^{18}O=Re(=^{16}O)$_2$, and a double substituted-^{18}O species, (^{18}O=)$_2$Re=^{16}O, where the 990 cm^{-1} band grows at the expense of 1002 cm^{-1}. Furthermore, the 960 cm^{-1} vibration, which becomes distinct after prolonged exposure to isotopic oxygen and at the expense of the ~1002 and 990 cm^{-1} bands, is tentatively attributed to the triple substituted-^{18}O species, (^{18}O=)$_3$Re. It is expected that if complete isotopic oxygen exchange were achieved beyond what is presented in curve D of Figure 1.7 (right), the 990 cm^{-1} would completely disappear and be replaced with the triply substituted (^{18}O=)$_3$Re band at 960 cm^{-1}. For the initial ν_{as}(Re(=^{16}O)$_3$) band at 977 cm^{-1}, isotopic exchange shifts the band to 932 cm^{-1} and a shoulder at 918 cm^{-1}, where both vibrations are tentatively assigned to a fully exchanged ν_{as}(Re(=^{18}O)$_3$) vibration with various degrees of distortion. The detection of four surface rhenia isotopic vibrations (Re(=^{16}O)$_3$ at 1010 cm^{-1}, Re(=^{18}O)(=^{16}O)$_2$ at ~1002 cm^{-1}, Re(=^{18}O)$_2$(=^{16}O) at 990 cm^{-1}, and Re(=^{18}O)$_3$ at 960 cm^{-1}) is consistent with the trioxo structure of the dehydrated surface ReO$_4$ species on SiO$_2$.

The *in situ* Raman spectra of the dehydrated supported Re$_2$O$_7$/TiO$_x$/SiO$_2$, Re$_2$O$_7$/ZrO$_x$/SiO$_2$, and Re$_2$O$_7$/AlO$_x$/SiO$_2$ catalysts are presented in Figure 1.8
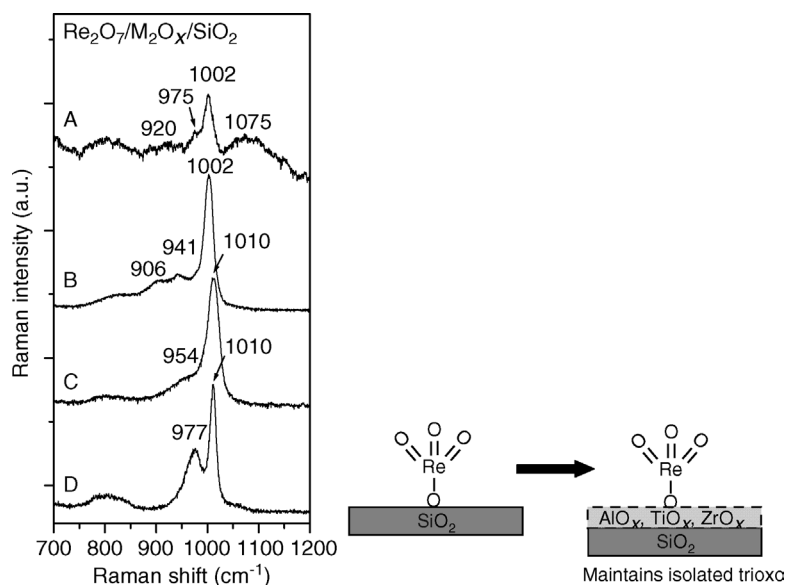
Figure 1.8 (Left) *In situ* Raman spectra (325 nm) of dehydrated supported (A) 3% Re$_2$O$_7$/TiO$_x$/SiO$_2$, (B) 3% Re$_2$O$_7$/ZrO$_x$/SiO$_2$, (C) 3% Re$_2$O$_7$/AlO$_x$/SiO$_2$, and (D) 3% Re$_2$O$_7$/SiO$_2$ (532 nm for 3% Re$_2$O$_7$/TiO$_x$/SiO$_2$ only) under oxidizing conditions at 450 °C. (Right) Schematic of dehydrated supported ReO$_x$ species on SiO$_2$ and on surface-modified silica.

(left) and give rise to strong bands at $\sim$1002–1010 cm^{-1} that is characteristic of the trioxo $v_s(Re(=O)_3)$ functionality [88]. The corresponding asymmetric stretch appears between 941 and 975 cm^{-1} for the surface-modified SiO$_2$ catalysts. The bridging Re−O−Ti and Re−O−Zr vibrations are also observable at $\sim$905–920 cm^{-1}. The similar band positions of the v_s and $v_{as}(Re(=O)_3)$ and bending mode of the model and surface-modified supported rhenia catalysts show that the surface oxide additives do not significantly alter the structure of the dehydrated surface ReO$_x$ species that consists of the terminal trioxo Re(=O)$_3$ functionality (see schematic in Figure 1.8 (right)).

1.8
Electronic Structure of Dehydrated Supported MO$_x$/SiO$_2$ and M$_1$O$_x$/M$_2$O$_x$/SiO$_2$ Catalysts via *In Situ* UV–Vis Spectroscopy

The corresponding UV–Vis DRS complements the surface Raman and IR spectroscopic vibrational information and provided local structural information (isolated monomer, dimer, polymeric chain, cluster, or 3D structure) of the supported metal oxide species. UV–Vis DRS monitors the surface metal oxide cation electronic structure via the ligand-to-metal charge transfer (LMCT) band position and the corresponding edge energy (E_g) value. The E_g values of the surface metal oxide species are determined by comparison against the electronic structures of well-defined metal oxide reference compounds [105–107]. In addition, each supported MO$_x$/SiO$_2$ catalyst system possesses unique spectral signatures through the LMCT band maxima that provide additional insights into their local molecular structures. It should be noted that the absorbance of a strong M$_2$O$_x$ species, such as TiO$_x$ for surface-modified TiO$_x$/SiO$_2$, may strongly overlap the contribution of the M$_1$O$_x$ species, such as the Re$_2$O$_7$/TiO$_x$/SiO$_2$. Therefore, careful baseline subtraction must be performed to ensure proper band deconvolution. The *in situ* UV–Vis E_g values for the dehydrated surface M$_1$O$_x$ (M$_1$ = V, Mo, and Re) species on native SiO$_2$ and surface-modified SiO$_2$ catalyst samples are scaled against well-defined reference compounds in Figure 1.9.

The dehydrated model supported M$_1$O$_x$/SiO$_2$ catalysts predominantly exist as isolated surface MO$_x$ species on SiO$_2$, which is reflected by the relatively high UV–Vis E_g values in Figure 1.9. The addition of the surface modifiers retains the high E_g values. For the surface molybdena catalyst system, the introduction of the surface M$_2$O$_x$ modifiers eliminates the higher wavenumber, or lower energy, LMCT transition in the UV–Vis spectra for the surface M$_1$O$_x$ species, which suggests a more isolated or distorted surface molybdena species [88]. This is in agreement with the Raman observations of the distortions of the surface MoO$_x$ species in supported MoO$_x$/M$_2$O$_x$/SiO$_2$ catalysts and the suppression of the surface monoxo species. The lack of influence of the different surface M$_2$O$_x$ ligands on the dehydrated surface O$_3$V=O and ORe(=O)$_3$ species reveals that these structures are not perturbed by the surface modification of the SiO$_2$ support.
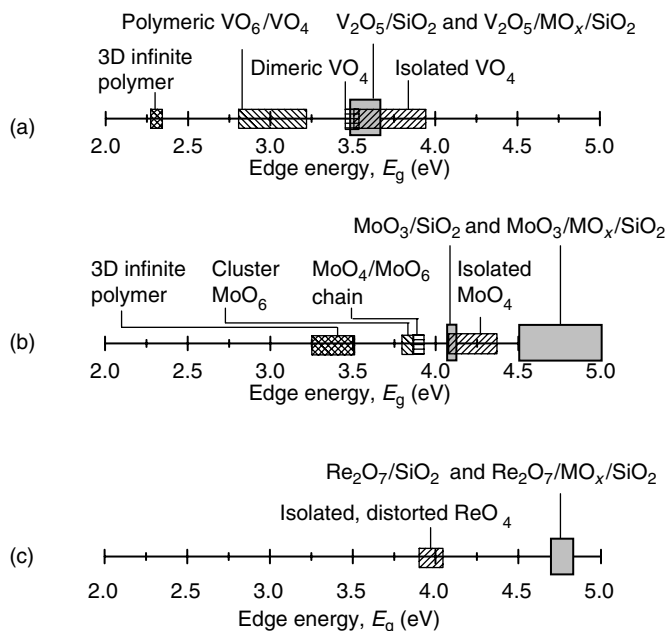
Figure 1.9 UV–Vis DRS edge energy, E_g, scale for well-defined reference compounds and measured E_g values for dehydrated SiO_2-supported (A) VO_x [108–114], (B) MoO_x [115–120], and (C) ReO_x [115, 121–124] catalysts.

1.9
Determination of Surface Kinetic Parameters

The surface chemistry and reactivity of model supported MO_x/SiO_2 and $M_1O_x/M_2O_x/SiO_2$ catalysts can be determined by CH_3OH-TPSR spectroscopy since CH_3OH is a "smart" chemical probe molecule capable of distinguishing between surface acidic, redox, and basic sites [125]. By determining the nature of the catalytic active sites (redox, acidic, or basic), their specific surface reactivity (k_{rds}) toward methanol can be calculated, where k_{rds} represents the first-order kinetic constant of the rate-determining step (rds) [125–128]. The dissociative chemisorption of methanol forms surface methoxy (CH_3O^*) intermediate species, which is the most abundant reaction intermediate (MARI) [129, 130], and undergoes different reaction pathways that are dependent on the nature of the catalytic active site: formaldehyde (HCHO) from surface redox sites, dimethyl ether (CH_3OCH_3, DME) from surface acidic sites, and CO/CO_2 from surface basic sites [125, 131]. H_2O formation is also a product of the CH_3OH surface chemistry. For the purposes of a focused discussion in this chapter, only the redox surface reactivity arising from methanol oxidative dehydrogenation to formaldehyde will be elaborated upon henceforth.

The surface kinetic parameters (E_{act} and k_{rds}) for the surface methoxy reactions to HCHO are directly obtained from the CH_3OH-TPSR spectra. The rds for the

unimolecular surface CH_3O^* dehydrogenation to HCHO involves breaking of the surface methoxy C−H bond [34]. Applying the first-order Redhead equation [132] for the unimolecular decomposition reaction of the rds for the different reaction pathways allows for the determination of the E_{act} for the surface reactions:

$$\frac{E_{act}}{RT_p^2} = \left(\frac{\upsilon}{\beta}\right)\exp\left(\frac{-E_{act}}{RT_p}\right) \tag{1.2}$$

in which T_p is the CH_3OH-TPSR peak temperature of the reaction product, R is the gas constant ($1.987\,cal\,mol^{-1}\,K^{-1}$), $\upsilon = 10^{13}\,s^{-1}$ for first-order kinetics, and β is the heating rate ($10\,°C\,min^{-1}$). The rate-determining step, k_{rds} (HCHO), for the conversion of the surface methoxy intermediate to HCHO is also a function of E_{act} (and hence T_p) and is determined by

$$k_{rds} = \upsilon \exp\left(\frac{-E_{act}}{RT}\right) \tag{1.3}$$

in which T is the reference temperature ($T = 230\,°C$) that will be used for comparison of k_{rds} values.

1.10
Redox Surface Reactivity of Model Supported M_1O_x/SiO_2 Catalysts

The specific catalytic activities (k_{rds}) for the formation of HCHO of the model supported M_1O_x/SiO_2 and surface-modified M_2O_x/SiO_2 catalysts were determined with CH_3OH-TPSR and are compared to their corresponding unsupported bulk MO_x catalysts in Figures 1.10. The surface reactivity of the model silica-supported M_1O_x catalytic active sites is affected by anchoring of the M_1O_x transition metal oxides to the SiO_2 support. The specific activity of the surface M_1O_x ($M_1 = V$ or Mo) catalytic active sites on SiO_2 is generally lower, by several orders of magnitude, than that of their unsupported M_1O_x metal oxides. The same is also true for the supported ZrO_x species on SiO_2. Whereas the surface AlO_x on silica is not affected by its anchoring to the SiO_2 support, with both exhibiting no redox activity, the surface TiO_x species on SiO_2 possess redox behavior while bulk TiO_2 does not exhibit redox characteristics. These differences reflect the changes resulting from anchoring isolated surface MO_x species onto the SiO_2 support surface via the bridging M−O−Si linkages. Although some contribution may come from the different molecular structures present in the bulk and supported MO_x catalysts, the coordination of the surface M_1O_x and M_2O_x species to the silica support appears to be the major influence on the reactivity characteristics of the surface oxide anchored to the SiO_2 support.

1.11
Redox Surface Reactivity of Supported M_1O_x/M_2O_x/SiO_2 Catalysts

The introduction of the surface AlO_x, TiO_x, and ZrO_x modifiers onto the SiO_2 support dramatically enhances the k_{rds} redox values, by as much as a factor of $\sim 10^4$, of the
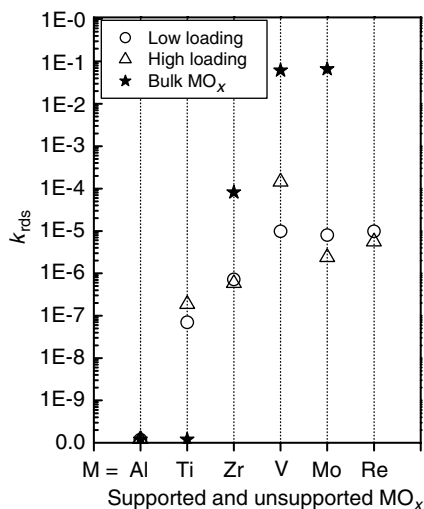
Figure 1.10 The k_{rds} values for HCHO formation from supported M_1O_x/SiO_2 and M_2O_x/SiO_2 catalysts at 230 °C for low and high (maximum dispersion) metal oxide coverage. The k_{rds} values of the unsupported bulk oxides are also shown for reference (with the star notation) [125–128].

supported M_1O_x catalytic active sites, as presented in Figure 1.11. These results are in agreement with steady-state CH_3OH oxidation studies, where the turnover frequency (TOF) significantly increases with the addition of the surface modifiers for the supported $M_1O_x/M_2O_x/SiO_2$ catalyst systems.
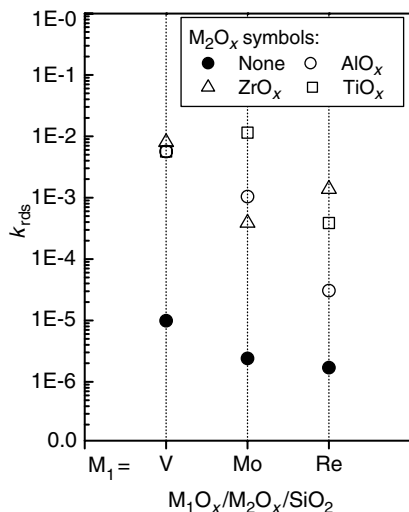
Figure 1.11 The k_{rds} values for supported 3% M_1O_x/5% M_2O_x/ SiO_2 catalysts ($M_1 = V$, Mo, and Re; $M_2 = Al$, Zr, and Ti) for decomposition of surface methoxy intermediate to HCHO.

Combining the molecular structural information with the corresponding reactivity studies allows for examination of possible molecular/electronic structure–activity relationships for the group 5–7 supported M_1O_x active sites. The multilayered supported $VO_x/M_2O_x/SiO_2$ and $ReO_x/M_2O_x/SiO_2$ catalyst systems contain the same surface monoxo VO_4 and trioxo ReO_4 structures, respectively, as their M_1O_x/SiO_2 counterparts. Consequently, the difference in reactivity is not related to a structural change of the surface M_1O_x species but is due to the different support ligands (M_2O_x and SiO_2). It is proposed that the enhanced surface redox activity is most likely related to the lower electronegativity of substrate oxide cations ($Si > Al > Ti \sim Zr$). Lowering of the oxide support ligand electronegativity increases the electron density on the oxygen of the bridging $M_1O_x-O-M_2O_x$ bond, which facilitates the disssociative chemisorption of methanol and decomposition of the surface methoxy intermediate to HCHO [133]. Several recent theoretical DFT/*ab initio* calculations have concluded that for the supported vanadia catalytic systems, the bridging $V-O-$support bond is the most energetically favorable methanol chemisorption site on the surface VO_x structure [84, 85, 134]. The bridging $V-O-$support bond has been shown to dramatically affect the steady-state TOF, defined as the number of HCHO molecules formed per surface VO_x sites per second [135] during steady-state CH_3OH oxidation. The TOF increases by two orders of magnitude with different supports, from 10^{-3} to $10^{-1}\,s^{-1}$ ($SiO_2 \ll Al_2O_3 \ll TiO_2 < ZrO_2$). Therefore, by substituting the bulk SiO_2 support with oxide ligands of lower electronegativity, the activity of the surface-modified vanadia catalyst systems was enhanced due to the formation of the bridging $V-O-Al$, $V-O-Zr$, and $V-O-Ti$ bonds, which are the favorable active sites for methanol chemisorption. In addition, anchoring of the surface M_1O_x species onto the surface M_2O_x species may also change their local molecular structures and their related surface reactivity properties.

1.12
Conclusions

It is shown in this chapter that the activity of the supported catalytic active sites can be controlled and designed by oxide ligands. The molecular and electronic characterization of the model supported MO_x/SiO_2 and surface-modified supported $M_1O_x/M_2O_x/SiO_2$ catalyst systems were determined by *in situ* Raman and UV–Vis spectroscopy, respectively. The *in situ* Raman spectroscopy measurements were undertaken using various new approaches, such as time-resolved spectroscopy under reductive (H_2) and isotopic exchange ($^{18}O-^{16}O$ and D_2O-H_2O) environments. These new findings revealed that supported V_2O_5/SiO_2 system contains isolated monoxo $V=O$ surface species, supported MoO_3/SiO_2 consists of both isolated monoxo $M=O$ and dioxo $O=Mo=O$ surface species, and supported Re_2O_7/SiO_2 possesses isolated trioxo $Re(=O)_3$ surface species. The redox activity of these surface M_1O_x species is significantly reduced by their anchoring to the SiO_2 support. The oxide ligands of the surface-modified SiO_2 catalysts, on the other hand, did not significantly alter the molecular structures of the model systems, but did significantly increase the catalytic redox

reactivity performance by as much as a factor of $\sim 10^4$. This enhancement in redox surface activity is through the bridging M−O−support bonds and their relative electronegativity. The lower cation electronegativity values of the M_2O_x oxide ligands increase the electron density of the oxygen atom in the bridging M_1O_x−O−M_2O_x and, consequently, enhance its proton-accepting characteristics (CH_3O−H during chemisorption and $^*OCH_2$−H during the surface decomposition step).

Acknowledgments

References

1 McDaniel, M.P. (1985) *Advances in Catalysis*, **33**, 47.

2 Burwell, R.L., Haller, G.L., Taylor, K.C. and Read, J.F. (1969) *Advances in Catalysis*, **20**, 1.

3 Mol, J.C. and Mouljin, J.A. (1987) *Catalysis – Science and Technology*, Vol. 8 (eds J.R. Anderson and M. Boudart), Springer-Verlag, Berlin, p. 69.

4 Grzybowska-Swierkosz, B. and Haber, J. (1984) *Vanadia Catalysts for Processes of Oxidation of Aromatic Hydrocarbons*, Polish Scientific Publications, Warsaw.

5 Bosch, J. and Jansen, F. (1988) *Catalysis Today*, **2**, 369.

6 Knozinger, H. (1989) Proceedings of the 9th International Congress Catalysis, Calgary, Vol. 5 (eds. M.J. Phillips and M. Ternan), The Chemical Institute of Canada, Ottawa, p. 20.

7 Prins, R., de Beer, V.H.J. and Somorjai, G.A. (1989) *Catalysis Reviews – Science and Engineering*, **31**, 1.

8 Hall, W.K. (1986) *Chemistry and Physics of Solid Surfaces* (eds. R. Vanselow and R.F. Howe), Springer-Verlag, Berlin, p. 73.

9 Topsoe, H. (1983) *Surface Properties and Catalysis by Non-Metals* (eds. J.P. Bonnelle, B. Delmon and E. Derouane), Reidel, Dordrecht, p. 329.

10 Delmon, B. (1979) Proceedings of the 3rd International Conference on Chemistry and Uses of Molybdenum (eds. H.F. Barry and P.C.H. Mitchell), Climax Molybdenum Company, Ann Arbor, MI, p. 73.

11 Gates, B.C., Katzer, J.R. and Schuit, G.C.A. (1979) *Chemistry of Catalytic Processes* (eds. R. Ciofallo, J. Marschall and B. Leap), McGraw-Hill, New York, p. 390.

12 Wachs, I.E., Saleh, R.Y., Chan, S.S. and Chersich, C.C. (1985) *Applied Catalysis A: General*, **15**, 339.

13 Grabowski, R., Grzybowska, B., Haber, J. and Sloczynski, J. (1975) *Reaction Kinetics and Catalysis Letters*, **2**, 81.

14 Deo, G. and Wachs, I.E. (1994) *Journal of Catalysis*, **146**, 323.

15 Mariscal, R., Galan-Fereres, M., Anderson, J.A., Alemany, L.J., Palacios, J.M. and Fierro, J.L.G. (1995) *Environmental Catalysis* (eds G. Centi *et al.*), SCI, Rome, p. 223.

16 Amiridis, M.D. and Solar, J.P. (1996) *Industrial & Engineering Chemistry Research*, **35**, 978.

17 Wauthoz, P., Machej, T. and Grange, P. (1991) *Applied Catalysis A: General*, **69**, 149.

18 Vogt, E.T.C., Boot, A., van Dillen, A.J., Geus, J.W., Janssen, F.J.J.G. and van den Kerkhof, F.M.G. (1988) *Journal of Catalysis*, **114**, 313.

19 Galan-Fereres, M., Mariscal, R., Alemany, L.J. and Fierro, J.L.G. (1994) *Journal of the Chemical Society, Faraday Transactions*, **90**, 3711.

20 De Boer, M., Van Dillen, A.J., Koningsberger, D.C., Geus, J.W., Vuurman, M.A. and Wachs, I.E. (1991) *Catalysis Letters*, **11**, 227.

21 Spencer, N.D., Pereira, C.J. and Grasselli, R.K. (1990) *Journal of Catalysis*, **126**, 546.

22 Banares, M.A., Fierro, J.L.G. and Moffat, J.B. (1993) *Journal of Catalysis*, **142**, 406.

23 Mel, J.C. and Moulijn, J.A. (1987) *Catalysis: Science and Technology*, Vol. 8 (eds. J.R. Anderson and M. Boudart), Springer-Verlag, Berlin, p. 69.

24 Xiaoding, X., Boelhouwer, C., Vonk, D., Benecke, J.I. and Mol, J.C. (1986) *Journal of Molecular Catalysis*, **36**, 47.

25 Banks, R.L. (1984) *Olefin Metathesis: Technology and Application. Applied Industrial Catalysis* (ed. B.E. Leach), Academic Press, New York, p. 215.

26 Haukka, S., Lakomaa, E. and Root, A. (1993) *The Journal of Physical Chemistry*, **97**, 5085.

27 Morrow, B.A. and Mcfarlan, A.J. (1990) *Journal of Non-Crystalline Solids*, **120**, 61.

28 Klaas, J., Schulz-Ekloff, G. and Jaeger, N.I. (1997) *The Journal of Physical Chemistry. B*, **101**, 1305.

29 Yoshida, S., Takenaka, S., Tanaka, T., Hirano, H. and Hayashi, H. (1996) Eleventh International Congress on Catalysis, *Studies in Surface Science and Catalysis*, 101, 871.

30 Srinivasan, S., Datye, A.K., Hampden-Smith, M., Wachs, I.E., Deo, G., Jehng, J.M., Turek, A.M. and Peden, C.H.F. (1991) *Journal of Catalysis*, **131**, 260.

31 Srinivasan, S., Datye, A.K., Smith, M.H. and Peden, C.H.F. (1994) *Journal of Catalysis*, **145**, 565.

32 Deo, G., Turek, A.M., Wachs, I.E., Huybrechts, D.R.C. and Jacobs, P.A. (1993) *Zeolites*, **13**, 365.

33 Fernandez, A., Leyrer, J., Gonzalez-Elipe, A.R., Munuera, G. and Knozinger, H. (1988) *Journal of Catalysis*, **112**, 489.

34 Mariscal, R., Palacios, J.M., Galan-Fereres, M. and Fierro, J.L.G. (1994) *Applied Catalysis A: General*, **116**, 205.

35 Hanprasopwattana, A., Rieker, T., Sault, A.G. and Datye, A.K. (1997) *Catalysis Letters*, **45**, 165.

36 Hanprasopwattana, A., Srinivasan, S., Sault, A.G. and Datye, A.K. (1996) *Langmuir*, **12**, 3173.

37 Galan-Fereres, M., Alemany, L.J., Mariscal, R., Banares, M.A., Anderson, J.A. and Fierro, J.L.G. (1995) *Chemistry of Materials*, **7**, 1342.

38 Tian, H., Ross, E.I. and Wachs, I.E. (2006) *The Journal of Physical Chemistry. B*, **110**, 9593.

39 Das, N., Eckert, H., Hu, H., Wachs, I.E., Walzer, J.F. and Feher, F.J. (1993) *The Journal of Physical Chemistry*, **97**, 8240.

40 Gao, X., Bare, S.R., Weckhuysen, B.M. and Wachs, I.E. (1998) *The Journal of Physical Chemistry. B*, **102**, 10842.

41 Oyama, S.T., Went, G.T., Lewis, K.B., Bell, A.T. and Somorjai, G.A. (1989) *The Journal of Physical Chemistry*, **93**, 6786.

42 Resini, C., Montanari, T., Busca, G., Jehng, J.M. and Wachs, I.E. (2005) *Catalysis Today*, **99**, 105.

43 Banares, M.A., Cardoso, J.H., Agullo-Rueda, F., Correa-Bueno, J.M. and Fierro, J.L.G. (2000) *Catalysis Letters*, **64**, 191.

44 Gao, X. and Wachs, I.E. (2002) *Topics in Catalysis*, **18**, 243.

45 Went, G.T., Oyama, S.T. and Bell, A.T. (1990) *The Journal of Physical Chemistry*, **94**, 4240.

46 Burcham, L.J., Datka, J. and Wachs, I.E. (1999) *The Journal of Physical Chemistry. B*, **103**, 6015.

47 Baltes, M., Kytokivi, A., Weckhuysen, B.M., Schoonheydt, R.A., van der Voort, P. and Vansant, E.F. (2001) *The Journal of Physical Chemistry. B*, **105**, 6211.

48 Kim, D.S. and Wachs, I.E. (1993) *Journal of Catalysis*, **142**, 166.

49 Jehng, J.-M., Tung, W.-C., Huang, C.-H. and Wachs, I.E. (2007) *Microporous and Mesoporous Materials*, **99**, 299.

50 Tanaka, T., Nojima, H., Yamamoto, T., Takenaka, S., Funabiki, T. and Yoshida, S. (1999) *Physical Chemistry Chemical Physics*, **1**, 5235.

51 Weckhuysen, B.M., Wachs, I.E. and Schoonheydt, R.A. (1996) *Chemical Reviews*, **96**, 3327.

52 Doornkamp, C., Clement, M., Gao, X., Deo, G., Wachs, I.E. and Ponec, V. (1999) *Journal of Catalysis*, **185**, 415.

53 Banares, M.A., Hu, H. and Wachs, I.E. (1995) *Journal of Catalysis*, **155**, 249.

54 Jehng, J.M., Hu, H., Gao, X. and Wachs, I.E. (1996) *Catalysis Today*, **28**, 335.

55 Lee, E.L. and Wachs, I.E. (2007) *The Journal of Physical Chemistry. C*, **111**, 14410.

56 Lee, E.L. and Wachs, I.E. (2008) *The Journal of Physical Chemistry. C*, **112**, 6487.

57 Mestl, G. and Srinivasan, T.K.K. (1998) *Catalysis Reviews – Science and Engineering*, **40**, 451.

58 Wachs, I.E. (2005) *Catalysis Today*, **100**, 79.

59 Brown, F.R., Makovsky, L.E. and Rhee, K.H. (1977) *Applied Spectroscopy*, **31**, 563.

60 Brown, F.R., Makovsky, L.E. and Rhee, K.H. (1977) *Journal of Catalysis*, **50**, 162.

61 Brown, F.R., Makovsky, L.E. and Rhee, K.H. (1977) *Journal of Catalysis*, **50**, 385.

62 Thomas, R., Moulijn, J.A. and Kerkhof, F.P.J.M. (1977) *Recueil des Travaux Chimiques des Pays-Bas*, **96**, 134.

63 Roozeboom, F., Mittelmeijer-Hazeleger, M.C., Moulijn, J.A., Medema, J., De Beer, V.H.J. and Gellings, P.J. (1980) *The Journal of Physical Chemistry*, **84**, 2783.

64 Roozeboom, F., Medema, J. and Gellings, P.J. (1978) *Zeitschrift fuer Physikalische Chemie*, **111**, 215.

65 Kerkhof, F.P.J.M., Moulijn, J.A. and Thomas, R. (1979) *Journal of Catalysis*, **56**, 279.

66 Chan, S.S., Wachs, I.E., Murrell, L.L., Wang, L. and Hall, W.K. (1984) *The Journal of Physical Chemistry*, **88**, 5831.

67 Cheng, C.P., Ludowise, J.D. and Schrader, G.L. (1980) *Applied Spectroscopy*, **34**, 146.

68 Wang, L. and Hall, W.K. (1983) *Journal of Catalysis*, **82**, 177.

69 Stencel, J.M., Makovsky, L.E., Sarkus, T.A., De Vries, J., Thomas, R. and Moulijn, J.A. (1984) *Journal of Catalysis*, **90**, 314.

70 Stencel, J.M., Makovsky, L.E., Diehl, J.R. and Sarkus, T.A. (1984) *Journal of Raman Spectroscopy*, **15**, 282.

71 Weckhuysen, B.M., Jehng, J.-M. and Wachs, I.E. (2000) *The Journal of Physical Chemistry. B*, **104**, 7382.

72 Banares, M.A. and Wachs, I.E. (2002) *Journal of Raman Spectroscopy*, **33**, 359.

73 Nakamoto, K. (1986) *Infrared and Raman Spectra of Inorganic and Coordination Compounds*, 4th edn, John Wiley & Sons, New York, NY.

74 Banwell, C.N. (1983) *Fundamentals of Molecular Spectroscopy*, 3rd edn, McGraw-Hill, London.

75 Busca, G. (2002) *Journal of Raman Spectroscopy*, **33**, 348.

76 Galeener, F.L. and Mikkelsen, J.C. Jr. (1981) *Physical Review B: Condensed Matter*, **23**, 5527.

77 Gao, X. and Wachs, I.E. (2000) *Journal of Catalysis*, **192**, 18.

78 Gao, X. and Wachs, I.E. (1999) *Catalysis Today*, **15**, 233.

79 Gao, X., Bare, S.R., Fierro, J.L.G., Banares, M.A. and Wachs, I.E. (1998) *The Journal of Physical Chemistry. B*, **102**, 5653.

80 Yudaev, I.V., Gan, Z., Paukshtis, E.A., Wachs, I.E. and Lapina, O.B., unpublished.

81 Turek, A.M., Wachs, I.E. and DeCanio, E. (1992) *The Journal of Physical Chemistry*, **96**, 5000.

82 Sanderson, R.T. (1988) *Journal of Chemical Education*, **65**, 112.

83 Ostromecki, M.M., Burcham, L.J. and Wachs, I.E. (1998) *Journal of Molecular Catalysis A: Chemical*, **132**, 59.

84 Dobler, J., Pritzsche, M. and Sauer, J. (2005) *Journal of the American Chemical Society*, **127**, 10861.

85 Magg, N., Immaraporn, B., Giorgi, J.B., Schroeder, T., Baumer, M., Dobler, J., Wu, Z., Kondratenko, E., Cherian, M., Baerns, M., Stair, P.C., Sauer, J. and Freund, H.J. 2004 *Journal of Catalysis*, **226**, 88.

86 Avdeev, V.I. and Zhidomirov, G.M. (2004) *Research on Chemical Intermediates*, **30**, 41.

87 Lee, E.L. and Wachs, I.E. (2008) *Journal of Catalysis*, **258**, 103.

88 Lee, E.L. and Wachs, I.E. (1991) *The Journal of Physical Chemistry*, accepted.

89 Gao, X., Fierro, J.L.G. and Wachs, I.E. (1999) *Langmuir*, **15**, 3169.

90 Gao, X., Bare, S.R., Fierro, J.L.G. and Wachs, I.E. (1999) *The Journal of Physical Chemistry B*, **103**, 618.

91 Banares, M.A., Spencer, N.D., Jones, D. and Wachs, I.E. (1994) *Journal of Catalysis*, **146**, 204.

92 Hardcastle, F.D. and Wachs, I.E. (1991) *The Journal of Physical Chemistry*, **95**, 10763.

93 Desikan, A.N., Huang, L. and Oyama, S.T. (1991) *The Journal of Physical Chemistry*, **95**, 10050.

94 Williams, C.C., Ekerdt, J.G., Jehng, J.-M., Hardcastle, F.D., Turek, A.M. and Wachs, I.E. (1991) *The Journal of Physical Chemistry*, **95**, 8781.

95 Hu, H., Wachs, I.E. and Bare, S.R. (1995) *The Journal of Physical Chemistry*, **99**, 10897.

96 Banares, M.A., Hu, H. and Wachs, I.E. (1994) *Journal of Catalysis*, **150**, 407.

97 Cornac, M., Janin, A. and Lavalley, J.C. (1986) *Polyhedron*, **5**, 183.

98 Seyedmonir, S.R. and Howe, R.F. (1988) *Journal of Catalysis*, **110**, 216.

99 Ohler, N. and Bell, A.T. (2005) *The Journal of Physical Chemistry. B*, **109**, 23419.

100 Chempath, S., Zhang, Y. and Bell, A.T. (2007) *The Journal of Physical Chemistry. C*, **111**, 1291.

101 Wachs, I.E. (1996) *Catalysis Today*, **27**, 437.

102 Vuurman, M.A. and Wachs, I.E. (1992) *The Journal of Physical Chemistry*, **96**, 5008.

103 Vuurman, M.A., Stufkens, D.J. and Oskam, A. (1992) *Journal of Molecular Catalysis*, **76**, 263.

104 Kim, D.S. and Wachs, I.E. (1993) *Journal of Catalysis*, **141**, 419.

105 Weber, R.S. (1995) *Journal of Catalysis*, **151**, 470.

106 Gao, X. and Wachs, I.E. (2000) *The Journal of Physical Chemistry. B*, **104**, 1261.

107 Ross-Medgaarden, E.I. and Wachs, I.E. (2007) *The Journal of Physical Chemistry. C*, **111**, 15089.

108 Wachs, I.E., Chen, Y., Jehng, J.-M., Briand, L.E. and Tanaka, T. (2003) *Catalysis Today*, **78**, 13.

109 Wright, A.C. (1984) *Philosophical Magazine B*, **50**, L23.

110 Ng, H.N. and Calvo, C. (1972) *Canadian Journal of Chemistry*, **50**, 3619.

111 Busca, G., Ricchiardi, G., Sam, D.S.H. and Volta, J.C. (1994) *Journal of the Chemical Society, Faraday Transactions*, **90**, 1161.

112 Marumo, F., Isobe, M., Iwai, S. and Kondo, Y. (1974) *Acta Crystallographica*, **B30**, 1628.

113 Evans, H.T. (1960) *Zeitschrift fur Kristallographie*, **114**, 257.

114 Gopal, R. and Calvo, C. (1974) *Acta Crystallographica*, **B30**, 2491.

115 Wachs, I.E. (2005) Molecular structures of surface metal oxide species: nature of catalytic active sites in mixed metal oxides, in *Metal Oxides: Chemistry and Applications* (eds. J.L.G. Fierro and H. Heinemann), CRC Taylor & Francis Press.

116 Wells, A. (1984) *Structural Inorganic Chemistry*, Oxford University, London.

117 Greenwood, N.N. and Earnshaw, A. (1989) *Chemistry of the Elements*, Pergamon Press, Elmsford, NY.

118 Knopnadel, I., Hartl, H., Hunnius, W.D. and Fuchs, J. (1974) *Angewandte Chemie International Edition*, **86**, 894.

119 Hove, A.R., Bildsoe, H., Skibsted, J., Brorson, M. and Jakobsen, H.J. (2006) *Inorganic Chemistry*, **45**, 10873.

120 Hardcastle, F.D. and Wachs, I.E. (1990) *Journal of Raman Spectroscopy*, **21**, 683.

121 Spitaler, J., Ambrosch-Draxl, C., Nachbaur, E., Belaj, F., Gomm, H. and Netzer, F. (2003) *Physical Review B: Condensed Matter*, **67**, 115127.

122 Lock, C.J.L. and Turner, G. (1975) *Acta Crystallographica*, **B31**, 1764.

123 Pendharkar, A.V. and Mande, C. (1973) *Pramana*, **1**, 104.

124 Swainson, I.P. and Brown, R.J.C. (1997) *Acta Crystallographica*, **B53**, 76.

125 Badlani, M. and Wachs, I.E. (2001) *Catalysis Letters*, **75**, 137.

126 Wang, X. and Wachs, I.E. (2004) *Catalysis Today*, **96**, 211.

127 Kim, T., Burrows, A., Kiely, C.J. and Wachs, I.E. (2007) *Journal of Catalysis*, **246**, 370.

128 Wachs, I.E., Jehng, J.-M. and Ueda, W. (2005) *The Journal of Physical Chemistry. B*, **109**, 2275.

129 Burcham, L.J., Briand, L.E. and Wachs, I.E. (2001) *Langmuir*, **17**, 6164.

130 Burcham, L.J., Deo, G., Gao, X. and Wachs, I.E. (2000) *Topics in Catalysis*, **11/12**, 85.

131 Tatibouet, J.M. (1997) *Applied Catalysis A: General*, **148**, 213.

132 Redhead, P.A. (1962) *Vacuum*, **12**, 213.

133 Kim, T. and Wachs, I.E., Ph.D. Thesis.

134 Bronkema, J.L. and Bell, A.T. (2007) *The Journal of Physical Chemistry. C*, **111**, 420.

135 Boudart, M. (1995) *Chemical Reviews*, **95**, 661.